Chapter III

Impact of energetic ion irradiation on Gd$_2$O$_3$ nanorods and interrelated optical emission and spin-spin relaxation feature

Rare-earth (RE) oxides, both in micro and nanoscale form, have drawn significant interest in the field of high performance luminescent devices, magnets and catalysts because of the fact that, its optoelectronic response emerge chiefly from participation of inter-shielded $4f$ electrons [1]. The device properties also depend strongly on chemical composition, crystal structure, shape as well as dimensionality of the system [2]. The lanthanide elements, in particular, exhibit remarkable optoelectronic and magnetic properties. They also act as promising candidate for deployment in nuclear technology as radiation tolerant ceramics [3, 4]. Among rare-earth sesquioxide based phosphors, gadolinium oxide (Gd_2O_3) has taken the lead to host transition metal (TM) and even the RE ions of desired interest. Apart from excellent optoelectronic response, nano-dimensional Gd_2O_3 has already demonstrated its immense potential in biomedical applications, e.g., in magneto-resonance imaging replacing traditionally used gadolinium chelates [5, 6].

On the other hand, ion irradiation is an excellent technique that is capable of manifesting structural and morphological properties in a controlled manner. The energetic ions deliver energy through different energy loss mechanisms: electronic (S_e) and nuclear (S_n). The electronic energy loss is due to the inelastic collision of incident ions with the atoms of the target material and becomes dominant in the MeV scale of energy regime (>1 MeV/nucleon) [7]. The nuclear energy loss is due to the elastic collision of the incident ions and becomes effective in the low energy regime (a few keV/nucleon) [8, 9]. There are several reports in the literature regarding oxide nanostructured systems which highlights irradiation induced modification of structural and optical responses [10,11]. The disintegration of rodlike structure of ZnO nanostructures into spherical nanoparticles has been observed as a result of MeV scale ion impact in a recent work [12]. On the other hand, the impact of ion irradiation has also been analyzed for stable RE sesquioxides [3,13]. Moreover, β-irradiation effect on oxide glasses and with TM and RE inclusions, was shown to the block development of defects in the host [14]. Owing to excellent thermal and mechanical stability of the RE oxides, studies as regards morphological

evolution and shape alteration have not been focused when subjected to MeV scale energetic irradiation.

This chapter presents microstructural and morphological characteristics of sol-hydrothermally grown Gd_2O_3 nanorods and irradiated by swift energetic ions. An attempt has been made to connect defect-mediated optical emission and spin–spin relaxation associated with charged oxygen vacancies (V_O^+) in ion-irradiated Gd_2O_3 nanorod systems.

3.1 Irradiation of Gd_2O_3 nanorod systems

First, the synthesized Gd_2O_3 nanorods are dispersed in a freshly prepared 5% wt polyvinyl alcohol (PVA) matrix media and with a ~50% volume dispersion. The nanorod- dispersed PVA films (thickness ~40 µm) are then casted on laboratory grade, sodium borosilicate glass slides (1×1 cm²) for the irradiation experiment. The samples are irradiated in a high vacuum chamber (pressure~10^{-6} mbar) using 80 MeV C^{6+} ion beams (with a beam current of ~1 pnA, particle nanoampere) available from a 15UD tandem accelerator of Inter University Accelerator Centre (IUAC), New Delhi (Appendix V). In order to ensure homogeneous irradiation condition, the ion beam was first scanned over a thick quartz plate of size 1×1 cm² fixed at the extreme end of the rectangular sample ladder. The ion fluence could be estimated by integrating the ion charge on the sample ladder, insulated from the chamber. With a dominant electronic energy loss of the chosen ions over the nuclear energy loss, the ion fluence is varied in the range of $1×10^{11}$- $3×10^{12}$ ions/cm². The energy of the ions is chosen in such a way that, the projectile range (R_P) of the ions is good enough to make ions pass through the target material without stop. It may be noted that, in any embedded system, both the matrix as well as the dispersed objects (nanorods) experience differently on subsequent impact of ions during irradiation. Using the SRIM 2008 program [15], the electronic energy loss (S_e), nuclear energy loss (S_n) and the projectile range (R_P) of the projectile ions were estimated and presented in Table 3.1.

3.1.1. Characterization techniques employed

Both un-irradiated and irradiated Gd_2O_3 nanorod samples are characterized by different analytical instruments. The structural characterization of pristine nanorods was performed by a Rigaku miniFlex X-ray diffractometer (XRD) that employs a copper target (CuK_α, λ=1.543 Å). The diffraction intensity was monitored corresponding to the Bragg's diffraction angle (2θ) varied in the range of 25-60°, and while considering a scanning rate of 2°/min and at a step angle of 0.05°. Transmission electron microscopy (TEM) imaging was performed by a JEOL JEM 2100 machine, operating at an accelerating voltage of 200 kV. In HRTEM measurement, a sliced specimen was first dispersed in the DI water, and then subjected to ultra-sonication, for 1 h. Prior to measurement, a micro drop of the sample was placed on the carbon coated copper grid. The Raman spectra of the samples have been recorded on a Renishaw In-Via Raman spectrometer (Renishaw, Wottonunder- Edge, UK) with an Ar⁺ laser line (λ =514·5 nm) as the excitation source and with a detector resolution of 0.3 cm⁻¹.

3.1.2 Structural and morphological evolution

The XRD patterns of the pristine and 80 MeV carbon ion irradiated Gd_2O_3 nanorods are shown in Figure 3.1 (a) (i-iv). As can be found, the pristine nanorod powder is characterized by four prominent peaks located at ~28.60°, 33.20°, 47.60° and 56.30° which corresponded to (222), (400), (440) and (622) crystallographic planes of the cubic phase (type-C) of the Gd_2O_3 system [16]. The PVA dispersed Gd_2O_3 nanorods subjected to irradiation at moderate fluences gave relatively noisy diffraction peaks (Figure 1a (ii,iii)). However, sharp peaks are regained at very high fluence owing to recovery from matrix encapsulation (Figure 3.1a (iv)). It may be noted that, we have performed the experiment on solid films of PVA dispersed with nano-Gd_2O_3. Under ion irradiation, the polymer matrix was believed to have damaged through breakage of covalent bonds due to excessive heating. On the other hand Gd_2O_3 is relatively resistant to ion irradiation. Thus nanorods can become free from matrix-encapsulation upon irradiation. Moreover, the diffraction peaks experienced a noticeable shifting toward higher Bragg angles owing to

introduction of adequate microstrain in the system. The average crystallite size (d) and microstrain (η) can be calculated using the popular Williamson-Hall (W-H) expression as mentioned in equation (2.1). While the average crystallite sizes vary in the range of 5.4-8.6 nm, the calculated microstrain is of the order of 10^{-3}, the values being presented in Table 3.2.
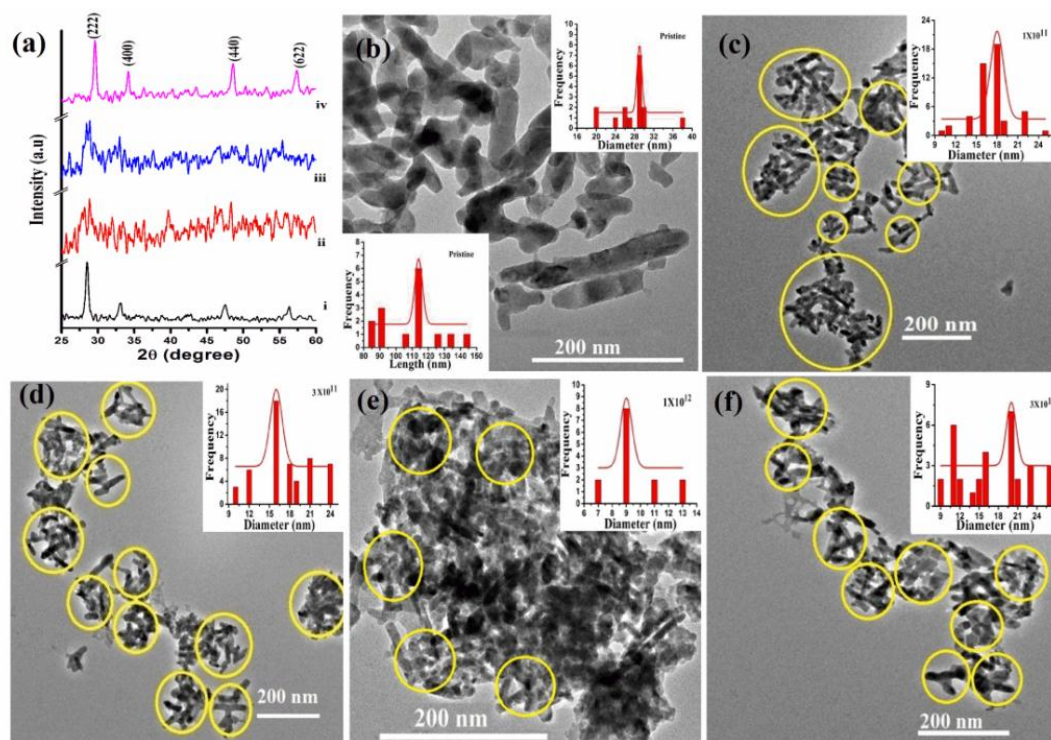

Figure 3.1: (a) XRD patterns of the (i) pristine and irradiated Gd₂O₃ nanorods at fluences of (ii) 1×10¹¹, (iii) 3×10¹¹ and (iv) 1×10¹² ions/cm². The HRTEM imaging of (b) pristine and irradiated (c) 1×10¹¹, (d) 3×10¹¹, (e) 1×10¹² and (f) 3×10¹² ions/cm² Gd₂O₃ nanorods. The histograms, shown as figure inset, represent size distribution of the nanorods.

Table 3.1: Electronic energy loss (S_e), nuclear energy loss (S_n) and the projected range (R_p) of 80 MeV C⁶⁺ ions in different material systems.

Material	S_e(eV/Å)	S_n (eV/Å)	Projectile range (μm)
PVA	27.91	1.528×10^{-2}	174.63
Gd₂O₃	78.31	4.319×10^{-2}	68.48
PVA-Gd₂O₃	51.35	2.828×10^{-2}	102.02

Table 3.2: Energy deposition and structural parameters associated with the Gd₂O₃ nanorods subjected to 80 MeV C⁶⁺ ion irradiation (through XRD and TEM analyses)

Ion fluence, φ (ions/ cm²)	Energy absorbed (J/cm²)	Average crystallite size, d (nm)	Micro-strain, ε (x 10³)	Lattice parameter (Å)	Average dimension of the nanorods		
					Length, L (nm)	Diameter, D (nm)	Aspect ratio (L/D)
0	0	6.46	-0.89	10.82	114	29	3.9

1×10^{11}	1.28	8.41	-1.55	10.78	83.9	17.9	4.6
3×10^{11}	3.84	5.68	-1.22	10.82	53	16	3.3
1×10^{12}	12.8	5.4	-7.9	10.53	34.9	9	3.8
3×10^{12}	38.4	-	-		74.1	20	3.7

The visual information as regards irradiation effect on Gd₂O₃ nanorods can be found in Figure 3.1 (b-f). The average diameter of the rods, for each fluence case, can be assessed from the figure-insets depicted in the form of histogram plots. With an average length of ~114 nm and diameter ~29 nm, the un-irradiated rods initially possessed an aspect ratio of ~3.9 (Figure 3.1(b)). When subjected to a low fluence (1×10^{11} ions/cm²) irradiation, both the average length (~83.9 nm) and diameter (~18 nm) get substantially reduced with the evidence of clustering effect (Figure 3.1(c)). As the fluence is increased (up to 1×10^{12} ions/cm²), both the length and diameter of the rods, in fact, experienced a decreasing trend along with pronounced bunching of rods well separated from each other (Figure 3.1(c) - (e)). The fluence dependent nanorod dimension and aspect ratio features are presented in Table 3.2. In particular, the aspect ratio (L/D) of our irradiated Gd₂O₃ nanorods, vary between ~3.3 and 4.6 and did not give any special trend with ion fluence variation (Table 3.2).

It may be noted here that, compared to other known oxides, the RE oxides are mechanically, chemically and thermally stable at large. The irradiated nanorods, in the present case, therefore not necessarily be melted wholly because of the ion impact. But normal impact of ions at the edges and surfaces can result in the dislodgement of atoms owing to sudden rise in temperature locally. The ion induced massive transport of the atoms from the nanorod surfaces could lead to apparently diminishing dimension of the Gd₂O₃ nanorods, which later existed in the form of bunch. The number of bunching patterns is likely to increase with the ion fluence, until a critical limit is achieved. We also witnessed a noticeable deformation in the shape of nanorods as a result of irradiation at a fluence of 1×10^{12} and 3×10^{12} ions/cm² (Figure 3.1(e) and (f)). The unusual development of tamarind- shaped nanostructures is highlighted in an enlarged micrograph, shown in Figure 3.2(a) and (b).

For the sake of comparison, a digital image of a few matured tamarinds is also provided (Figure 3.2(c)). On a comparative note, the un-irradiated nanorod has a smooth surface, while the irradiated one experienced a bumpy surface, as can be found in Figure 3.2(d),(e). Our samples were dispersed in polymer matrix, multiple cleaning steps (dilution, sonication etc.) were necessary prior imaging. The blurring effect could not be avoided, which might have arisen due to operational conditions or sample handling. Earlier banana shaped nanorods were shown to be produced with the help of femtosecond laser irradiation [17]. It was argued that the twin-plane, single crystal structure of the nanorods with surface defects might have helped transforming polycrystalline particles upon laser irradiation [17]. The transformation starts at the surface and then likely to propagate into the interior of the nanorods. Sun et al. have offered a qualitative account wrt structural and shape evaluation of different Gd₂O₃ and other RE oxides subjected to a plasma torch [18].
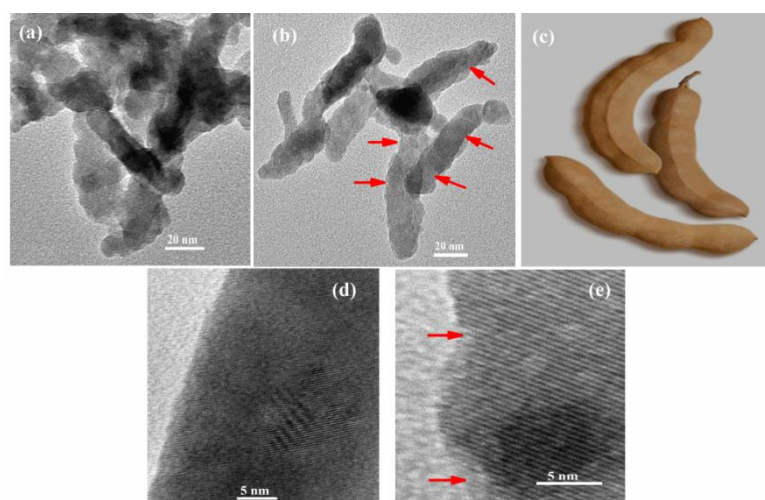

Figure 3.2: Tamarind-like shape evolution upon irradiation at a fluence of 1×10^{12} ions/cm² is depicted in (a), with regular deformation indicated by arrow marks for the case (b) 3×10^{12} ions/cm² , and (c) image on real look of mature tamarinds.(source: http://www.in.all.biz/img/in/catalog/23346.jpeg). The smooth and bumpy surface features can be visualized in magnified TEM images meant for the (d) un-irradiated nanorod and the one (e) irradiated at a fluence of 1×10^{12} ions/cm².

3.1.3 Raman spectroscopy analysis

Raman spectroscopy is an effective tool to investigate the phononic modes within a system under study. According to factor group theory analysis the optical and acoustic mode of cubic RE oxide can be expressed by [19]:

$$\Gamma_{op} = 4A_g + 4E_g + 14F_g + 5A_{2u} + 5E_u + 16F_u, \ \Gamma_{ac} = F_u, \tag{3.1}$$

where A_g, E_g and F_g are Raman active, F_u is IR active and A_{2u} and E_u are inactive. On the whole, 22 Raman modes have been predicted for the C-type RE sesquioxides [19]. The Raman spectra of pristine and 80 MeV carbon ion irradiated Gd_2O_3 nanorods are depicted in Figure 3.3. In RE sesquioxides, the strong Raman bands are normally observed in the range ~330 - 420 cm^{-1}. In the present case, apart from a strong peak at ~360 cm^{-1}, two subsidiary peaks located at ~313, and 446 cm^{-1} can be found. The peak at ~313 cm^{-1} is attributed to the mixed modes of F_g+E_g and the one at ~446 cm^{-1} could be due to an independent F_g mode [20]. The most prominent peak at ~360 cm^{-1} is assigned to the F_g+A_g mode, that characterize a sustained mixed mode present in the cubic phase of Gd_2O_3 [20]. The peak at ~360 cm^{-1} experiences a blue-shifting to ~375 cm^{-1} after ion irradiation. The full width at half maxima (FWHM) of the Raman peak (F_g+A_g mode) at 360   cm^{-1} has slightly decreased from a magnitude of ~21.7 cm^{-1} to 19.6 cm^{-1} as for the Gd_2O_3 nanorods irradiated at a very high fluence (3×10^{12} ions/cm^2).

The assigned Raman active mode is likely to be upshifted due to the inclusion of surface optic mode or other permissible mode of low frequency. Previously, shifting of the Raman peak to high frequency side was assigned to the reduction of particle size [21]. Since the post irradiated systems showed a significant reduction wrt the length and diameter of the nanorods, phonon confinement can be more effective which in turn led to the desired shift. The irradiation led creation of oxygen vacancies may also be responsible for shifting of the Raman peak. In general, any oxide system has plentiful oxygen vacancies in ambient conditions. In this regard, semiconductor oxides which are rich source of oxygen vacancies were shown to be responsible for shifting and broadening of the Raman peak positions [22]. The presence of oxygen related defects has also been ascertained through theoretical treatments, as discussed in the following section #3.1.4. Due to the generation of irradiation induced oxygen vacancies, the lattice is believed to be compressed locally at the nanorod surfaces, and consequently phononic modes are manifested.
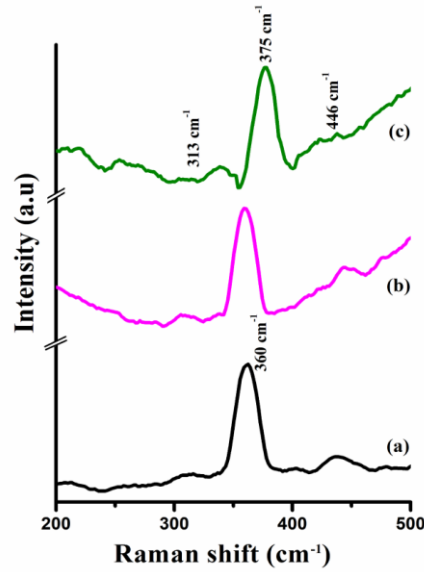
Figure 3.3: Raman spectra of a) pristine, and irradiated Gd$_2$O$_3$ nanorods at a fluence of b) 1x 10^{12} ions/cm^2, c) 3x 10^{12} ions/cm^2. Note the shifting of the prominent peak at very high fluence.

3.1.4 Theoretical treatment on energy deposition

Let's consider an ideal, one dimensional nanorod that consists of N number of atoms and that, the volume of the nanorod is equal to the total volume of the N atoms. If x_i (i=1, 2, 3…) is the atomic percentage of each element of diameter d_i (i=1, 2, 3…) present in the nanorod of diameter D and length L, then the number of atoms present in the nanorod will be given by [10]

$$N = \frac{1.5\, f\, D^2}{\sum x_i d_i^3} L \tag{3.2}$$

where f is the packing fraction ($\approx$0.68) of Gd$_2$O$_3$ [23] and $\sum x_i$=1. Knowing the respective atomic diameters of gadolinium and oxygen as, 0.18 nm and 0.06 nm, we find N=53.68 $D^2 L$.

It is believed that, the impact of a MeV scale ion will spread its energy while forming some cylindrical zones [10]. If δ and l are the diameter and length of any cylindrical zone, then the number of atoms that would be present in it can be given by:

$$n = \frac{N \delta^2 l}{D^2 L} \tag{3.3}$$

The amount of energy deposited during the thermal spike event refers to the product of the electronic energy loss (S_e) and electron–phonon coupling efficiency (g). The total energy deposited along the path of the projectile ion is,

gS_el and the amount of energy received by each of the atoms in the cylindrical region of diameter δ can be expressed as,

$$E = \frac{gS_e l}{\frac{N\delta^2 l}{D^2 L}}$$

$$E = \frac{gS_e D^2 L}{N\delta^2} \qquad\qquad (3.4)$$

Assuming $g\sim0.4$ [24] and using equation (3.4), the variation of the energy received per atom of the cylindrical regions can be plotted as a function of δ, which is shown in Figure 3.4(a).

Gd₂O₃ and yttrium oxide (Y₂O₃) are well known oxide systems in the RE family which share a number of physical properties. The respective lattice parameters (*a*) of cubic Gd₂O₃ and Y₂O₃ are 10.79 Å and 10.60 Å [25]. In Y₂O₃ system, the oxygen vacancy ($V\ddot{o}$) and yttrium vacancy (Vy''') related formation energies are predicted as, ~20.31 eV and 47.37 eV; respectively [25]. Assuming that, the formation energy of yttrium vacancy and gadolinium vacancies are close, the above mentioned energies correspond to the cylindrical regions of diameter (δ) ~0.53 nm and ~0.35 nm (indicated by * signs, Figure 3.4(a)). Since the number of atoms *n*, present in the cylindrical region is directly proportional to the square of δ as per eqn. (3.3), oxygen related defects are believed to be manifested, to a great extent.

3.1.5 Mechanism of formation of tamarind- shaped nanorods at a higher fluence

During irradiation both the matrix as well as (dispersed) nanoscale objects experience the impact of ions differently and to different extent. While polymer is believed to be damaged at high fluences, it is only the inorganic solid-state object which matter the most after irradiation. Earlier, ion irradiation led structural transition and shape evolution aspect was discussed independently in Gd₂O₃ and Gd₂TiO₅ systems [18, 26]. It is known that, a swift heavy ion while traversing through a material system, is capable of creating an ion track of typical diameter ~5 nm [27]. Earlier amorphous latent tracks of diameter ~5

nm have also been witnessed due to 74 MeV Kr ion irradiation on $Y_2Ti_2O_7$ nanoparticles in EP450 ODS steel [28].

In the present case, assuming that the nanorods are spread uniformly all throughout the matrix and remain normal to the ion impact, each of the nanorods is expected to receive quite uniform amount of ion exposure. Referring to the 1st fluence (1×10^{11} ions/cm^2), each of the nanorods is to receive about 11 independent normal impacts. Since the pristine nanorods are of approximate length ~116 nm, the impact of incoming ions, is likely to affect only up to ~55 nm of its total length (assuming the region of influence on the nanorod surface as, ~5 nm). This is, essentially suggest single ion impact feature with a fairly low chance of overlapping effect (multi ion impact). In this case, no shape deformation is predicted as evident from the HRTEM image (Figure 3.1 (c)). On a quantitative note, the respective number of ion impacts as for the 2nd (3×10^{11} ions/cm^2), 3rd (1×10^{12} ions/cm^2) and 4th (3×10^{12} ions/cm^2) fluences are ~32, 105 and 317. Accordingly, with an increasing fluence, the effective region of influence over the nanorod length can be increased to ~160, 525 and 1585 nm, provided that the single ion impact is ensured. But, since the apparent length of the nanorods is much shorter a very strong overlapping effect can be realized at very high (especially, 3rd and 4th) fluences causing multi-ion impact mechanism (Figure 3.4(b)). In contrast to the single ion impact regions, the multi-ion impact led overlapping of regions of influence at the nanorod surface sites is chiefly responsible for the dislodgement of sufficiently large number of atoms at regular intervals. Consequently, in view of flying off the surface atoms from the impact zones, the shape is deformed locally yet in regular intervals. The multi impact region may also experience localized pressure effect and contributing to shape manifestation. It is well known that, the rare earth Gd_2O_3 system is mechanically, chemically and thermally stable. Due to impact of ions on the nanorods, atoms on the surfaces of the nanorods tend to get dislodged as a result of which shape changes might occur. The overall impact on the nanorods give rise to aperiodic, distorted morphology which resemble tamarind-like shape evolution (Figure 3.2(a) and (b)). The

schematic representation on the manifested shape evolution of the Gd_2O_3 nanorods, has been illustrated in Figure 3.4 (b).
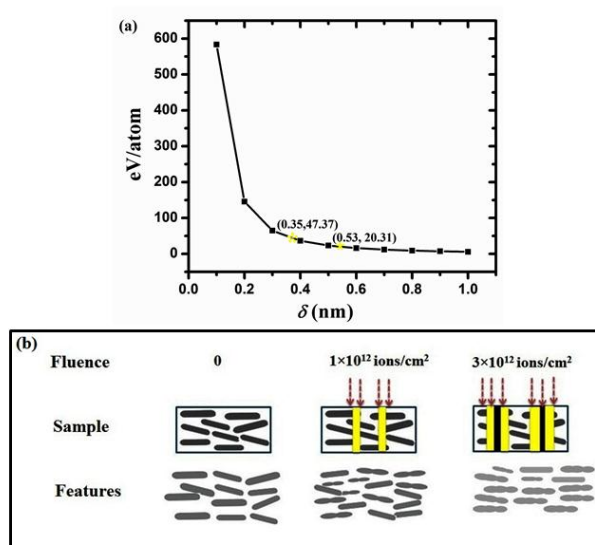

Figure 3.4: (a) Variation of energy deposited per atom during irradiation vs. effective diameter of cylindrical zones created due to swift ion impact, (b) scheme illustrating shape evolution of Gd_2O_3 nanorods as a result of overlapping effect accompanied by impact of multiple ions.

3.2 Interrelated optical emission and spin-spin relaxation response in Gd_2O_3 nanorods

In order to compare radiative emission and spin-spin interaction mediated by charged defects, both un-irradiated and irradiated Gd_2O_3 nanorod samples are analyzed by PL spectroscopy and EPR spectroscopy. While PL emission data is acquired from a PerkinElmer LS 55 luminescence spectrophotometer, the EPR study has been performed on a JES-FA200 ESR Spectrometer working in the X band (~9.44 GHz) and at a field modulation of 100 kHz, while offering a sensitivity of $7×10^9$ spins/0.1 mT, and resolution of 2.35 μT.

A single nanorod with lattice fringe pattern and a selective area electron diffraction pattern is shown in Figure 3.5(a). The EDX pattern on the other hand gave clear indication of Gd and O elements present in the system (Figure 3.5(b)).

The room temperature PL emission spectra (λ_{ex}=300 nm) of the un-irradiated and irradiated Gd_2O_3 nanorods are depicted in Figure 3.6(a). The

asymmetric nature of the luminescence spectra suggests that, the overall trace is the superimposition of several peaks originated through different radiative events. In order to extract individual peaks, the de-convolution was adopted on every spectrum by way of multi-peak Gaussian fitting employing OriginPro8.5® software. In the deconvolution process, the area under the experimental curve and the empirical curve are essentially same thereby representing the sum total of areas under each of the deconvoluted curves. Although the strength of emission was noticeably different, nearly unaltered emission positions have been identified both for the pristine and irradiated nanorods (Figure 3.6(b-f)). The deconvoluted PL spectrum of the un-irradiated nanorods is shown in Figure 3.6(b), whereas the characteristic curves of the irradiated nanorods are highlighted in Figure 3.6(c-f). The emission peak located at ~350 nm is attributed to the oxygen vacancies of neutral (V_{Ox}) kind [29]. Whereas, the deep blue band positioned at ~414 nm is assigned to the recombination of delocalized electrons in the vicinity of conduction band with a single charged state of surface oxygen vacancy V_O^+, in accordance with the proposition of Wang et al.[30]. The blue emission response at ~460 and ~491-518 nm have arisen owing to the surface defects mediated Schottky and Frenkel types [29]. The second band is assigned to the introduction of closely spaced surface energy states within the forbidden gap due to local departure from perfect periodicity and introduction of degeneracy.
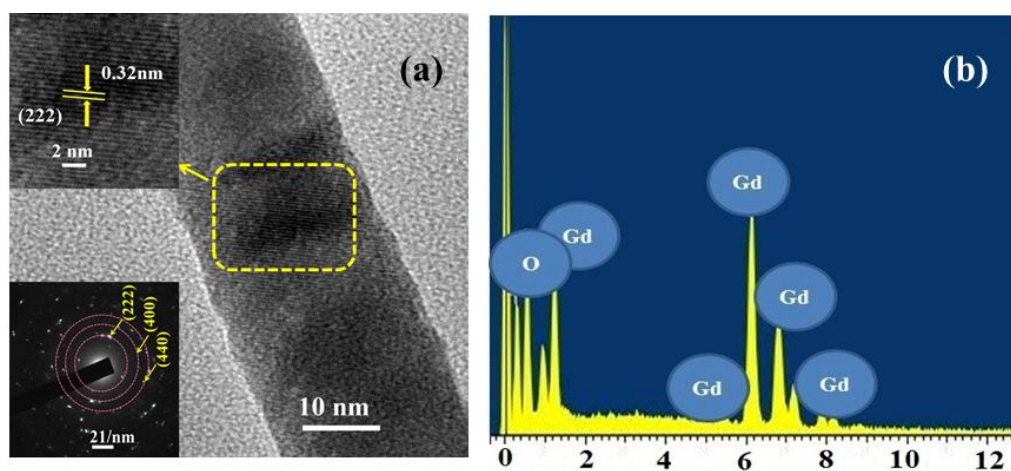

Figure 3.5: (a) A magnified view of an isolated nanorod with zoomed view of a segment highlighting lattice fringe and defects. The SAED pattern that highlights diffused diffraction rings is shown as inset of (a) at the bottom left. An EDX pattern illustrating elemental composition is depicted in Figure (b).
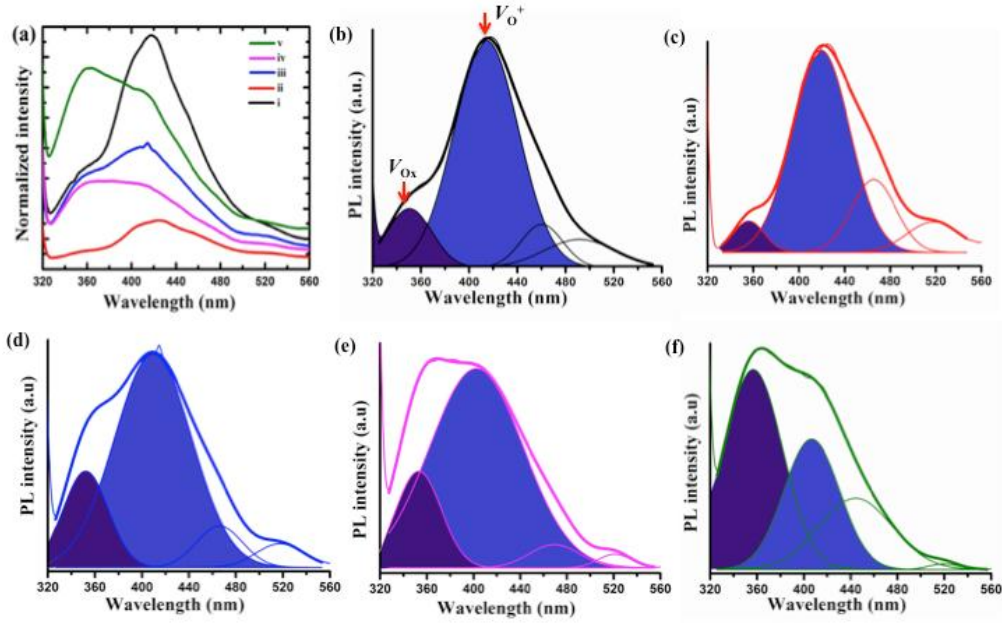
Figure 3.6: (a) PL spectra (λ_{ex} = 300 nm) of un-irradiated and irradiated Gd₂O₃ nanorod systems (i: 0, ii: 1×10^{11}, iii: 3×10^{11}, iv: 1×10^{12} and v: 3×10^{12} ions/cm²), and (b–f) deconvoluted PL spectra of the corresponding systems. Note the shadow areas under the curves which essentially represent mainly V_{Ox} and V_{O}^{+} defects mediated contributions.

The characteristic signal strength, line width (peak-to-peak width i.e., $\Delta H_{\text{p-p}}$), resonance field (H_R) and effective g (g_{eff}) values corresponding to the un-irradiated and irradiated Gd₂O₃ nanorods are evaluated from the first derivative EPR absorption spectra, shown in Figure 3.7(a, b). The observation of a fairly broad, symmetric EPR spectrum without unusual splitting signature discards the possibility of hyperfine splitting in the system under study. Moreover, the exchange interaction is expected to be small because, in Gd³⁺ ions, the inner 4f electrons are bound to the nucleus and shielded by the outer most electrons, $5s^2 5p^6$ via a crystal field [31]. The effective g-value can be calculated from the relation:

$$g_{eff} = hf / \mu_B H_R, \tag{3.5}$$

where f (=9.44 GHz) is the frequency of the microwave source, μ_B is the Bohr magnetron. At room temperature (RT), the g_{eff} values of the pristine and irradiated (fluence: 0, 1×10^{11}, 3×10^{11}, 1×10^{12} and 3×10^{12} ions/cm²) nanorods are estimated to be, ~2.037, 2.052, 2.06, 2.068 and 2.098 (Table 3.3). The low

temperature (LNT) data, however, give corresponding g_{eff} values as, 2.014, 2.009, 2.012, 2.012 and 1.902. It is worth mentioning here that, while $g_{eff} \geq 2$ mostly arise through spin contribution of holes, $g_{eff} < 2$ accounts for surface electron contributions [32].
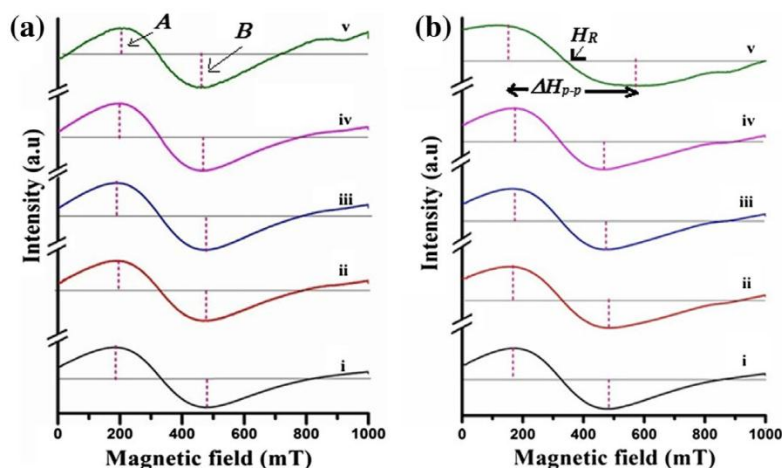

Figure 3.7: First-derivative EPR absorption spectra of the un-irradiated and irradiated Gd₂O₃ nanorods (i: 0, ii: 1×10^{11}, iii: 3×10^{11}, iv: 1×10^{12} and v: 3×10^{12} ions/cm²) acquired at (a) 300 K and (b) 77 K.

Table 3.3: Characteristic parameters as predicted from the analysis of the EPR spectra

Ion fluence (ions/cm²)	H_R (mT)		ΔH_{p-p} (mT)		g_{eff}		$\tau_{ss}(10^{-11}$ s)	
	RT (300K)	LNT (77K)	RT (300K)	LNT (77K)	RT (300K)	LNT (77K)	RT (300K)	LNT (77K)
0 (pristine)	331.25	325.63	294.52	311.82	2.0380	2.014	3.13	3.06
1×10^{11}	328.94	327.94	284.72	328.85	2.052	2.009	3.26	2.96
3×10^{11}	327.5	325.88	289.61	311.25	2.061	2.012	3.24	3.07
1×10^{12}	326.34	325.88	268.85	295.67	2.068	2.012	3.37	3.24
3×10^{12}	321.73	344.80	257.89	451.73	2.098	1.902	4.32	2.66

In all forms of spectroscopy, basically spectral lines are characterized by their signal strength (intensity), full width, and above all, position ignoring occurrence of multiplets. While intensity of the EPR absorption is proportional to the concentration of paramagnetic species available in the system, the width of resonance is dependent on the relaxation time of the spin state. If the line

width of the EPR signal is dictated by the spin–lattice interaction, it would decrease with decreasing temperature [33]. Since we observed an opposite trend, yet similar to the EPR response of Ce and Gd doped $NiFe_2O_4$ nanosystems [34], a dominant spin-spin relaxation is prevalent in our Gd_2O_3 nanorod-systems. The line-width of a typical EPR spectrum is given by:

$$\Delta H_{p-p} \propto \tau_{sl}^{-1} + \tau_{ss}^{-1} \; , \hspace{3cm} (3.6)$$

where τ_{sl} and τ_{ss} represent spin-lattice and spin-spin relaxation time constants; respectively [33]. Normally, $\tau_{sl} > \tau_{ss}$ and that, τ_{ss} tend to decline with the reduction of spin-spin separation i.e., by increasing spin concentration or paramagnetic centers. In the spin-spin relaxation process, the time constant (τ_{ss}) is normally determined from the peak–to-peak line width as [33, 34],

$$1/\tau_{ss} = \Delta H_{p-p} \left(\pi g / h \right) \mu_B \; . \hspace{3cm} (3.7)$$

Since intensity is directly linked to the concentration of paramagnetic centers, we intended to evaluate participation of V_O^+ in both PL emission and EPR absorption data. We plotted the relative PL intensity (V_{Ox}/V_O^+) of charged-to-neutral oxygen vacancies and spin-spin relaxation time (τ_{ss}) as a function of ion fluence. The estimated τ_{ss} values, as for room temperature cases, are presented along with the relative PL intensity depicted in Figure 3.8(a). The features, while exhibiting growing exponential trends, ensure a direct connection between the PL and EPR results. An apparently growing trend of 350 nm to 414 nm peaks with an increase in ion fluence signifies an improvement of neutral defects (V_{Ox}) over the singly charge defects (V_O^+). It may be noted that, in wide band gap oxides the presence of charged oxygen vacancies and cationic interstitials mostly contribute to donor states in the forbidden gap [35,36]. Here we anticipate that, the charged vacancies (V_O^+) get neutralized by free electron capture during prolonged ion irradiation. Alternatively, an adequate suppression of the V_O^+ paramagnetic centers with increasing ion fluence would increase the inter-spin distance (d), thereby enhancing τ_{ss} values (Figure 3.8(b)). Even though the spin-spin relaxation is drastically suppressed at RT, the τ_{ss} values (10^{-11}s) are smaller at $77K$ (liquid nitrogen temperature, LNT) than at RT (Table 3.3). This is because, unpaired spins present in the Gd_2O_3 nanorod

system experience slow relaxation at RT, but fast relaxation at LNT. A substantial amount of spins, which are infringed by thermal agitation at RT, become active at LNT. An adequate reduction of spin-spin separation and eventually, fast relaxation is quite feasible in a system with large spin concentrations that emerge from their unpaired existence. A comparative account on relative spin factor of irradiated samples with respect to pristine one, which were represented as F1, F2, F3, and F4 and estimated for RT and LNT environments, can be found in Figure 3.8(c) and (d).
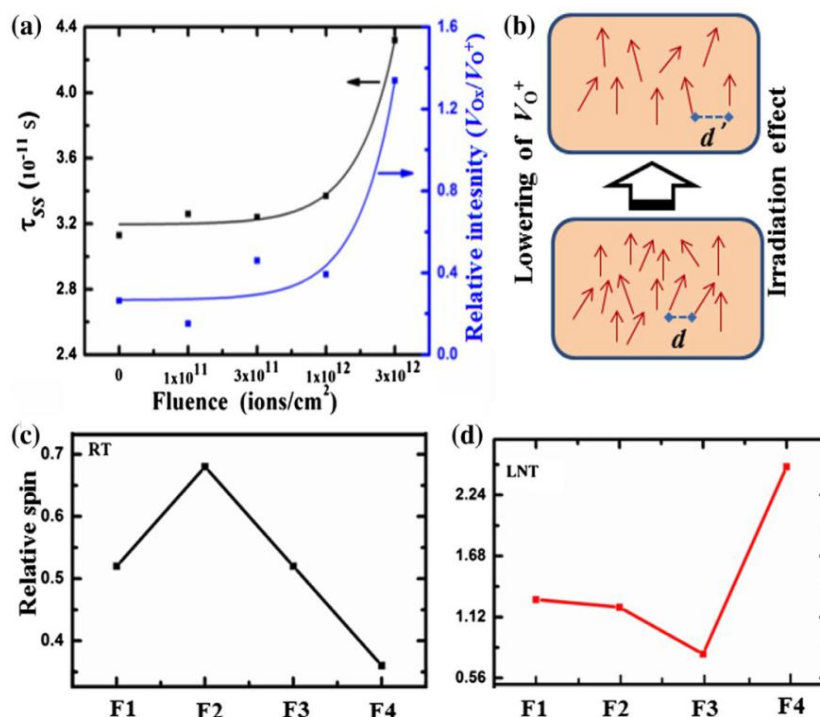

Figure 3.8: (a) Curves of relative PL intensity (V_{Ox}/V_O^+) and τ_{ss} with ion fluence, (b) schematic representation of V_O^+ mediated spin distribution (d'>d), d being the inter-spin separation in case of un-irradiated nanorods and d' that for irradiated systems. The spin factor was calculated with pristine sample as reference. The response of the irradiated nanorods, in RT and LNT environments, are highlighted in (c) and (d), respectively.

3.3 Concluding remarks

The impact of 80 MeV C^{6+} ions on the morphological evolution of one dimensional Gd₂O₃ nanorods has been discussed with a brief theoretical treatment. Shortening of nanorods, with aspect ratio varying between 3.3 and 4.7, was observed when the rods are subjected to irradiation. An unusual surface deformation with tamarind-like shape evolution is realized at a higher fluence ($>1\times10^{12}$ ions/cm²). In the Raman spectra of the nanorod system, a

prominent Raman peak located at ~360 cm^{-1} and assigned to the F_g+A_g mode, was observed to be blue-shifted in case of the nanorods subjected to a very high fluence ion exposure (3×10^{12} ions/cm²). The luminescence response of the cubic phase Gd$_2$O$_3$ nanorods exhibited several defect related emissions, including that mediated via neutral and charged oxygen vacancies. Upon irradiation, the V_O^+ defects which appear as the source of paramagnetic centers get suppressed, thereby increasing inter-spin separation. As predicted from PL data, with irradiation, V_O^+ defects get transformed to V_0. The reduction of V_O^+ defects is a consequence of decrease of concentration of paramagnetic centers and increase of spin-spin distance. Accordingly, a higher magnitude of spin-spin relaxation time, τ_{ss} has been realized due to longer relaxation trend. In contrast, owing to repressed thermal agitation and active spins, the τ_{ss} values are lowered at LNT than at RT.

References

[1] Hasegawa, Y., Thongchant, S., Wada, Y., Tanaka, H., Kawai, T., Sakata, T., Mori, H., and Yanagida, S. Enhanced Luminescence and Photomagnetic Properties of Surface-Modified EuO Nanocrystals. *Angew. Chemistry*, 114 : 2177-2179, 2002.

[2] Xu, Z. Yang, J., Hou, Z., Li, C., Zhang, C., Huang, S., Lin., J. Hydrothermal synthesis and luminescent properties of Y$_2$O$_3$:Tb^{3+} and Gd$_2$O$_3$:Tb^{3+} microrods. *Materials Research Bulletin*, 44: 1850-1857, 2009.

[3] Tang, M., Lu, P., Valdez, J. A., and Sickafus, K. E. Ion-irradiation-induced phase transformation in rare earth sesquioxides (Dy$_2$O$_3$, Er$_2$O$_3$, Lu$_2$O$_3$), *Journal of Applied Physics*, 99: 063514(1-7), 2006.

[4] Sickafus, K.E. Grimes, R. W., Valdez, J. A., Cleave, A., Tang, M., Ishimaru, M., Corish, S. M., Stanek, C.R., and Uberuaga, B. P. Radiation-induced amorphization resistance and radiation tolerance in structurally related oxides. *Nature Materials*, 6: 217-223, 2007.

[5] Zhou, L. Gu, Z., Liu, Xi., Yin, W., Tian, G., Yan, Li., Jin,S., Ren, W., Xing, G., Li, W., Chang, X., Hu, Z., and Zhao., Y. Size-tunable synthesis of lanthanide-doped Gd$_2$O$_3$ nanoparticles and their applications for optical and magnetic resonance imaging. *Journal of Materials Chemistry*, 22: 966-974, 2012.

[6] Park, J. Y., Baek, M. J., Choi, E. S, Woo, S., Kim, J. H., Kim,T. J., Jung, J. C., Chae, K. S., Chang, Y., and Lee, G. H. Paramagnetic ultrasmall gadolinium oxide nanoparticles as advanced T1 MRI contrast agent: Account for large longitudinal relaxivity, optimal particle diameter, and in vivo T1 MR images. *ACS Nano* 3: 3663-3669, 2009.

[7] Paul, N., Devi, M., and Mohanta, D. Synthesis, characterization and effect of low energy Ar ion irradiation on gadolinium oxide nanoparticles. *Materials Research Bulletin*, 46: 1296-1300, 2011.

[8] Lian, J. Zhou, W., Wei, Q. M., Wang, L. M., Boatner, L. A., and Ewing, R. C. Simultaneous formation of surface ripples and metallic nanodots induced by phase decomposition and focused ion beam patterning. *Applied Physics Letters,* 88: 093112 (1-3), 2006.

[9] Carter , G., and Vishnyakov, V. Roughening and ripple instabilities on ion-bombarded Si. *Physical Review B* , 54: 17647-17653,1996.

[10] Bayan, S. and Mohanta, D. Effect of 80MeV nitrogen ion irradiation on ZnO nanoparticles: Mechanism of selective defect related radiative emission features. *Nuclear Instruments and Methods in Physics Research Section B: Beam Interactions with Materials and Atoms,* 269: 374-379, 2011.

[11] Mohanta, D., Nath, S. S., Bordoloi, A., Choudhury, A., Dolui, S. K., and Mishra, N. C. Optical absorption study of 100-MeV chlorine ion-irradiated hydroxyl-free ZnO semiconductor quantum dots. *Journal of Applied Physics*, 92 : 7149-7152, 2002.

[12]Bayan, S. and Mohanta, D. Fragmentation of elongated-shaped ZnO nanostructures into spherical particles by swift ion impact. *Physica E: Low-dimensional Systems and Nanostructures*, 54: 288-294, 2013.

[13] Antic, B., Kremenovic, A., Draganic, I., Colomban, Ph., Radovic , D. V., Blanusa, J., Tadic , M., and Mitric, M. Effects of O^{2+} ions beam irradiation on crystal structure of rare earth sesquioxides. *Applied Surface Science,* 255: 7601-9704, 2009.

[14] Malchukova,E., Boizot, B., Petite G. and Ghaleb D. Irradiation effects in oxide glasses doped with transition and rare-earth elements, *European Physical*

Journal Applied Physics, 45 :10701,2009.

[15] Zeigler, J.F., Zeigler, M.D., and Biersack, J.P. SRIM (2008) - The Stopping and Range of Ions in Matter 2008, ⟨www.srim.org⟩.

[16] Hazarika, S. and Mohanta, D. Production and optoelectronic response of Tb^{3+} activated gadolinium oxide nanocrystalline phosphors. *European Physical Journal Applied Physics* ,62: 30401(p1-p5), 2013.

[17] Gordel, M., Banska, J. O., Matczyszyn, K., Nogues, C., Buckle, M., and Samoc, M. Post-synthesis reshaping of gold nanorods using a femtosecond laser. *Physical Chemistry Chemical Physics*, 16:71-78, 2014.

[18] Sun, X.L. Toka, A.I.Y., Huebnerb, R., and Boey, F.Y.C. Phase transformation of ultrafine rare earth oxide powders synthesized by radio frequency plasma spraying, *Journal of the European Ceramic Society*, 27: 125-130, 2007.

[19] Ubaldini, A., and Carnascialib M. M. Raman characterisation of powder of cubic RE_2O_3 (RE = Nd, Gd, Dy, Tm, and Lu), Sc_2O_3 and Y_2O_3. *Journal of Alloys and Compounds*, 454: 374-378, 2008.

[20] Rajan, G. and Gopchandran, K.G. Enhanced luminescence from spontaneously ordered $Gd_2O_3{:}Eu^{3+}$ based nanostructures. *Applied Surface Science,* 255: 9112-9123, 2009.

[21]Choi, H. C., Jung, Y. M., and Kim, S. B. Size effects in the Raman spectra of TiO_2 nanoparticles. *Vibrational Spectroscopy*, 37: 33-38, 2005.

[22] Parker, J. C., and Siegel R. W. Calibration of the Raman spectrum to the oxygen stoichiometry of nanophase TiO_2. *Applied Physics Letters*, 57: 943-945, 1990.

[23] Jacobsohn, L. G., Bennett, B. L., Muenchausen, R. E., Tornga, S. C., Thompson, J. D., Ugurlu, O., Cooke,D. W., and Sharma, A. L. L. Multifunction $Gd_2O_3{:}Eu$ nanocrystals produced by solution combustion synthesis: Structural, luminescent, and magnetic characterization. *Journal of Applied Physics,* 103: 104303(1-6),2008.

[24] Szenes, G., Pászti, F., Péter, A., and Popov, A.I. Tracks induced in TeO_2 by heavy ions at low velocities. *Nuclear Instruments and Methods in Physics*

Research B, 166-167: 949-953, 2000.

[25] Putilov, L.P., Varaksin, A.N., and Tsidilkovski V.I. Defect formation and water incorporation in Y_2O_3. *Journal of Physics and Chemistry of Solids*, 72:1090-1095,2011.

[26]Zhang, J., Zhang, F., Lang, M., Lu, F., Lian, J., and Ewinget, R. C. al. Ion-irradiation-induced structural transitions in orthorhombic Ln_2TiO_5. *Acta Materialia*, 61: 4191-4199, 2013.

[27] Fleischer, R.L., Price, P.B. and Walker, R.M. *Nuclear Tracks in Solids.* University of California Press, Berkeley, CA, 1975.

[28] Monnet, I., Grygiel, C., Lescoat, M.L., and Ribis, J. Amorphization of oxides in ODS steels/materials by electronic stopping power. *Journal of Nuclear Materials*, 424 :12-16, 2012.

[29] Dhananjaya, N., Nagabhushana , H., Nagabhushana , B.M., Rudraswamy , B., Sharma , S.C., Sunitha , D.V., Shivakumara , C., and Chakradhar R.P.S. Effect of different fuels on structural, thermo and photoluminescent properties of Gd_2O_3 nanoparticles. *Spectrochimica Acta Part A: Molecular and Biomolecular Spectroscopy*, 96: 532-540, 2012.

[30] Hu,C., Liu, H., Dong, W., Zhang, Y., Bao, G., Lao,C., and Wang, Z. L. $La(OH)_3$ and La_2O_3 nanobelts—synthesis and physical properties. *Advance Materials*, 19: 470–474, 2007.

[31] Srinivasulu, K., Omkaram, I., Obeid, H., Kumar, A. S., and Rao, J.L. Structural and magnetic properties of Gd^{3+} ions in sodium–lead borophosphate glasses. *Journal of Molecular Structure*, 1036: 63-70, 2013.

[32] Howe, R.F., and Gratzel, M. EPR study of hydrated anatase under UV irradiation. *Journal of Physical Chemistry*, 91: 3906-3909, 1987.

[33] Murphy D M. *EPR Spectroscopy of Polycrystalline Oxide Systems I: Metal Oxide Catalysis.* Weinheim: WILEY-VCHVerlag GmbH, 2009.

[34] Dixit, G., Singh , J. P., Srivastava , R.C., and Agrawal, H.M. Magnetic resonance study of Ce and Gd doped $NiFe_2O_4$ nanoparticles. *Journal of Magnetism and Magnetic Materials*, 324: 479-483, 2012.

[35] McCluskey, M.D. and Jokela, S. J. Defects in ZnO, *Journal of Applied Physics*, 106: 071101(1-13), 2009.

[36] Lin, B., Fu, Z., and Jia, Y. Green luminescent center in undoped zinc oxide films deposited on silicon substrates. *Applied Physics Letters,* 79 : 943-945, 2001.